



Research paper

Effective charge separation in site-isolated Pt-nanodot deposited PbTiO₃ nanotube arrays for enhanced photoelectrochemical water splitting

Chang Won Ahn^{a,1}, Pramod H. Borse^{b,1}, Ju Hun Kim^c, Jae Young Kim^c, Jum Suk Jang^d, Chae-Ryong Cho^e, Jang-Hee Yoon^f, Byoung-seob Lee^f, Jong-Seong Bae^f, Hyun Gyu Kim^{f,*}, Jae Sung Lee^{c,*}

^a Department of Physics and EHSRC, University of Ulsan, Ulsan 680-749, Republic of Korea

^b International Advanced Research Centre for Powder Metallurgy and New Materials, BalapurPO, Hyderabad, Telangana 500 005, India

^c School of Energy and Chemical Engineering, Ulsan National Institute of Science & Technology (UNIST), Ulsan 689-798, Republic of Korea

^d Division of Biotechnology, Safety, Environment and Life Science Institute, Chonbuk National University, Iksan 570–752, Republic of Korea

^e College of Nanoscience and Nanotechnology, Pusan National University, Busan 609-735 Republic of Korea

^f Korea Basic Science Institute, Busan Centre, Busan 609-735, Republic of Korea

ARTICLE INFO

ABSTRACT

Keywords:

Photoelectrochemical water splitting

PbTiO₃

Nanotube arrays

Electron-hole separation

Site isolation

Highly uniform, self-supported PbTiO₃ nanotube arrays are fabricated on a transparent conducting glass by an all solution-based, hard-templating procedure. A new concept of site-isolation has been realized by Pt-sol infiltration only in the internal core of deposited nanotube arrays and thus physically separating electron and hole reaction sites on inside and external surface of the nanotubes, respectively. The effective charge separation by the site-isolated Pt-nanodot deposited PbTiO₃ nanotube photoanode leads to greatly enhanced photocurrent generation and H₂ evolution efficiencies relative to those of the particulate-type photoanode or PbTiO₃ nanotube without Pt infiltration in photoelectrochemical water splitting under visible light. The physical site isolation through nano-engineering of the material fabrication is expected to offer an effective strategy for preparation of high-efficiency photoelectrochemical devices.

1. Introduction

The present-day synthetic technologies are capable of tuning the material properties at nano-dimensional regimes [1]. Thus, it is rewarding to exploit the nano-engineering capability to acquire the specific material properties required for desired applications [2]. An area that needs such an innovative material design is the hydrogen production via photocatalytic and photoelectrochemical solar water splitting [3]. Since the first demonstration of photoelectrochemical (PEC) water-splitting [4], TiO₂ has been studied extensively as a potential photocatalytic electrode material. Because TiO₂ absorbs only a limited part of solar spectrum due to a large band gap (3.2 eV), however, exhaustive search has been going on for efficient and economic photocatalytic materials [5].

An efficient photocatalytic material for water splitting should absorb ample visible light photons (of a small band gap), have a proper band alignment to oxidize or reduce water, and remain stable against the photocorrosion in water [4,6]. In view of commendable

photocatalytic properties of TiO₂, we are interested in visible-light absorbing, lead-containing titanates as potential photoelectrode materials for PEC water splitting such as PbBi₄Ti₄O₁₅ and PbTiO₃ that are known for their photocatalytic activity for water splitting [7]. The perovskite PbTiO₃, better known for its ferroelectricity, exists in two crystal structures; tetragonal phase (*P4 mm*) of $a = b = 3.9022$, $c = 4.1437 \text{ \AA}$ and cubic phase (*Pm-3m*) of $a = b = c = 3.887 \text{ \AA}$ [8]. Cubic PbTiO₃ exhibits a smaller band gap of 2.78 eV with well-aligned conduction and valence band edges favorable for redox reactions of H₂O molecule. It is important to note that our earlier work clearly demonstrated that a nearly complete substitution of Pb into layered perovskite family was a unique way to turn an only UV-active photocatalyst to a visible light-responsive one [9]. This was elucidated by the DFT-computed band structure that revealed that Pb 6s orbital interacted with O 2p orbital to raise the valance band edge position and thus to reduce the band gap energy [9,10]. Hence, in the present study, PbTiO₃ (PTO) is selected as the base photocatalytic material to fabricate nano-structured photoelectrode for PEC water splitting.

* Corresponding authors.

E-mail addresses: hhgkim@kbsi.re.kr (H.G. Kim), jlee1234@unist.ac.kr (J.S. Lee).

¹ These authors contributed equally to this work.

A photoelectrode made of PbTiO_3 particles usually generates much lower photocurrents than TiO_2 although it absorbs a larger fraction of the sunlight. Here we adopted two synthetic strategies to improve PEC performance of PTO. First, one-dimensional (1-D) nanotube arrays of PbTiO_3 (denoted as NT-PTO) was fabricated by a hard template method. In the nanotubes, electrons experience a quantum confinement in the transverse direction, and thus travel only in one direction along an axial quantum channel [11]. This would decouple the transport paths of electrons and holes and thus reduce their recombination. Further to augment the charge separation effect of NT-PTO, we infiltrated Pt nanodots only into the core of NT-PTO to obtain a ‘site-isolated’ Pt-dots@ PbTiO_3 nanotube array (PNT-PTO) that locates water oxidation sites (by holes) outside of the tube and reducing electrons toward inside core of the nanotube on their way to the FTO substrate [12].

This highly nano-engineered photoanode reduced the energy-wasteful electron-hole recombination, and thus enhanced efficiency in PEC water splitting relative to reference electrodes made of PbTiO_3 nanotubes (no Pt-dots) or PbTiO_3 powders (no nanotube). In the past, PbTiO_3 was shown to be a stable particulate photocatalyst for visible light water splitting as well as the photodegradation of organic pollutants. In a recent work, Reddy et al. reported synthesis of particulate form of Cu doped PbTiO_3 to produce hydrogen under visible light [13]. However, there is no report on use of nanotubular PbTiO_3 in PEC applications probably because of the synthetic difficulty of nanostructures at a high temperature needed to synthesize crystalline PbTiO_3 . Such a harsh synthesis condition is also bound to degrade the transparent conducting oxide glass like In:SnO₂ (ITO) or F:SnO₂ (FTO) that is used as a substrate [14].

2. Experimental section

2.1. Fabrication of AAO template and transfer onto FTO

In order to fabricate NT-PTO and PNT-PTO films, nanoporous anodic aluminum oxide (AAO) was used as a hard-template and the procedure is depicted in Fig. 1. First, an AAO template with a pore diameter of ~90 nm was prepared by using a two-step anodization process [2,15]. Aluminum foil and graphite served as the anode and cathode in the two-electrode electrochemical cell. A high-purity (99.998%) thin Al sheet (from Alfa Aesar) was electropolished in a mixture of ethanol and perchloric acid (4:1 vol ratio) at +18 V for 5 min creating a smooth Al surface. The shiny Al was anodized in 0.3 M oxalic acid at 50 V and 10 °C for 7 h. The formed Al_2O_3 layer was then removed in a mixture of chromic acid (1.8 wt%) and phosphoric acid

(6 wt%) at 60 °C for 3 h. A second anodization step followed in 0.3 M oxalic acid at 50 V and 10 °C for 3 h to grow highly ordered porous Al_2O_3 .

After the second anodization, a thin layer of polystyrene (PS) film was spin-coated on the surface of the AAO template at 3000 rpm for 30 s using a 2 wt% PS/CHCl₃ solution, and heated to 80 °C to evaporate the solvent. The thin PS layer plays an important role as a support in handling the thin AAO template to prevent mechanical deformations such as folding, cracking or ripping. The remaining Al was next removed by immersing in a saturated HgCl₂ aqueous solution for 6 h. To remove the barrier layer at the bottom of the AAO template and pore widening, the PS coated AAO templates were placed on the surface of a phosphoric acid solution (8.5 wt%) for 30 min. The thin AAO template was transferred onto the FTO substrate, and then PS layer was removed using CHCl₃. The thin AAO template exhibited good contact with the FTO substrate by van der Waals force between the AAO template and FTO substrate. This AAO template was used to form PTO nano-array over the FTO substrate.

2.2. Fabrication of Pt-dot deposited PbTiO_3 nanotube array photoanodes

For preparation of the PbTiO_3 precursor solutions, lead acetate trihydrate ($\text{Pb}(\text{C}_2\text{H}_3\text{O}_2)_2 \cdot 3\text{H}_2\text{O}$, Aldrich 99.99%) and titanium(IV) butoxide ($\text{Ti}[\text{O}(\text{CH}_2)_3\text{CH}_3]_4$, Aldrich 97%) were used as the starting chemicals, and 2-methoxy ethanol ($\text{C}_3\text{H}_8\text{O}_2$, Sigma-Aldrich 99.8%), and acetylacetone ($\text{C}_5\text{H}_8\text{O}_2$, Sigma-Aldrich 99%) were used as the solvent and the chelating agent, respectively. To compensate for the loss of Pb during thermal annealing, 10% excess of the Pb precursor was added. The concentration of PbTiO_3 in the final solution was adjusted to ~0.4 mol/L. To obtain PbTiO_3 nanotubes, the precursor solution was infiltrated into the AAO template on FTO by spin-coating with a rate of 3000 rpm for 30 s. The wet film was dried at 150 °C for 5 min on a hot plate. Subsequently, the dried gel films were calcined at 350 °C for 5 min and then annealed at 650 °C for 30 min in oxygen ambience. In order to infiltrate Pt into the cores of PbTiO_3 nanotubes, 10, 20, and 30 wt% H_2PtCl_6 /ethanol solutions were spin-coated onto PbTiO_3 /AAO/FTO glass at a rate of 3000 rpm for 30 s, and then annealed at 200 °C for 10 min. Finally, to remove the AAO template selectively, the annealed sample was etched in 5 wt% H_3PO_4 solution.

2.3. Physical characterization

The crystallinity of the annealed films was examined using glancing angle X-ray diffraction (XRD, Philips X'Pert). The microstructure of the films was investigated using a field emission scanning electron

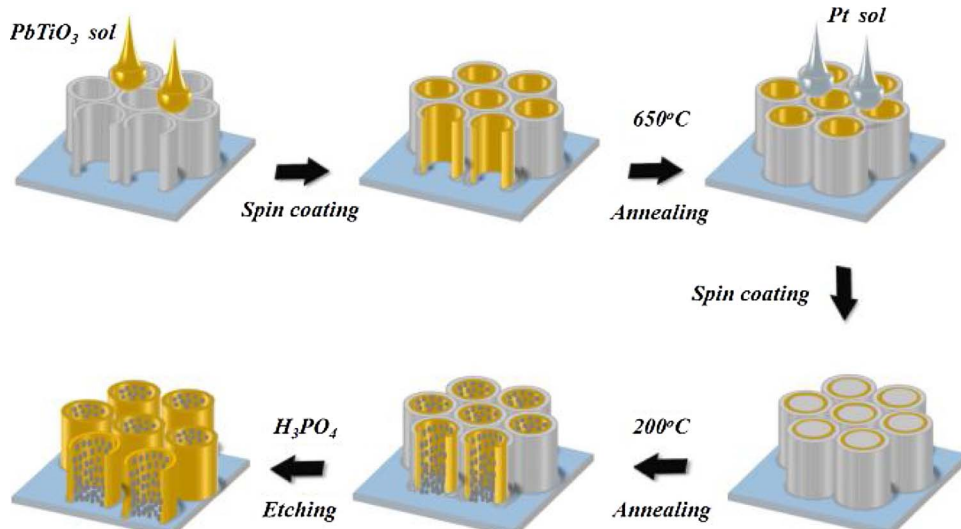


Fig. 1. Schematics showing the fabrication process of well-aligned Pt-dot deposited PbTiO_3 (PNT-PTO) arrays over a transparent conducting substrate (FTO).

microscope (FE-SEM, JSM-6500F, Jeol). The UV-vis absorbance was measured with a UV/Vis spectrometer (UV-2401PC, Shimadzu) to determine the band gap of the photocatalyst.

2.4 Electrochemical and Photoelectrochemical Measurements.

The photoelectrochemical properties of the Pt-modified PbTiO_3 nanotubes array were measured at applied potentials in 1.0 M KOH solution. The photocurrent (J) – potential (V) curves were recorded under $\lambda > 420$ nm irradiation obtained by using an optical filter along with a 300 W Xe-lamp (XC-300, ATAGO). The electrochemical and photoelectrochemical measurements were made on a potentiostat (DY2300, Digi-Ivy) in a standard three-electrode configuration with a platinum wire counter electrode, a saturated Ag/AgCl reference electrode, and a photoanode working electrode. The potential $V_{\text{Ag}/\text{AgCl}}$ was converted to the reversible hydrogen electrode (V_{RHE}) scale using the Nernst equation;

$$V_{\text{RHE}} = V_{\text{Ag}/\text{AgCl}} + 0.059 \text{pH} + V_{\text{Ag}/\text{AgCl}}^0$$

where $V_{\text{Ag}/\text{AgCl}}^0 = 0.1976$ V at 25 °C. In order to measure the rates of H_2/O_2 evolution, the gas phase of the reactor was analyzed under the chronoamperometry conditions with a bias voltage of 1.02 V_{RHE} . The gaseous product analysis was carried out by using a gas chromatograph (Agilent Technologies 7890A) equipped with a thermal conductivity detector (a molecular sieve 5 Å column and Ar carrier).

3. Results

3.1. Fabrication of site-isolated Pt-dot deposited PbTiO_3 nanotube arrays on FTO

The procedure to fabricate the site isolated PNT-PTO photoanode is described in Experimental Section and schematically depicted in Fig. 1. First, anodic aluminum oxide (AAO) with a pore diameter of ~90 nm was prepared by using a two-step anodization of an aluminum foil [15]. The thin AAO template was transferred onto the FTO substrate by supporting with a polystyrene layer that was removed later. The transfer of AAO without mechanical deformation is an important step to fabricate a transparent photoanode. Into the pores of this AAO template placed on FTO glass, the PbTiO_3 precursor solution was infiltrated by spin-coating. The film was annealed at 650 °C for 30 min in oxygen ambience to obtain PbTiO_3 nanotubes formed along the internal surface of AAO. In order to deposit Pt nanodots into PbTiO_3 nanotubes, H_2PtCl_6 solution was spin-coated onto $\text{PbTiO}_3/\text{AAO}/\text{FTO}$ glass and then annealed at 200 °C for 10 min. Since the external surface of PbTiO_3 nanotubes is still covered by AAO template, Pt can be deposited only on the inner surface. Finally, the annealed sample was etched in 5 wt.% H_3PO_4 solution to remove the AAO template and obtain the Pt-dots@ PbTiO_3 nanotubes/FTO (PNT-PTO) photoanode.

The FESEM images of AAO template and the formed PNT-PTO film are shown in Fig. 2a,b and Fig. S1 in Supplementary Material (SM). The AAO template exhibits exceptional uniformity of hexagonal pores of ~90 nm with little defects. The Pt-nanodot deposited NT-PTO also shows bundles of highly uniform nanotube of 90 nm in diameter and 5 nm-thick walls forming a well-aligned individual nanotube array on FTO substrate. As a control sample, PbTiO_3 powder was also made by a solid-state reaction from the same precursors as used in PbTiO_3 nanotubes synthesis but without the AAO template. Thus, obtained powder was used for screen printing over FTO substrate. High resolution TEM (HRTEM) images of particulate and PbTiO_3 nanotubes in Fig. 2c,d confirm highly crystalline cubic phase PbTiO_3 in both particulate and nanotube forms. The HRTEM images and the corresponding SAED patterns in insets show highly (110) oriented pattern of PbTiO_3 nanotubes. Indicated lattice fringes represent (100) (0.28 nm) and (110) (0.39 nm) planes of nanotube. Above results clearly demonstrate that a highly crystalline nanotube has been formed in particles as well as in nanotubes. The x-ray diffraction (XRD) pattern of the PbTiO_3 nanotubes array in Fig. 3a indicates the cubic perovskite structure of PbTiO_3 . The

UV-vis absorption spectrum in Fig. 3b shows an absorption edge at 446 nm corresponding to a band gap of 2.78 eV. The very sharp absorption edge of PbTiO_3 shows a good contrast with that of well-known N-doped TiO_2 ($\text{TiO}_{2-x}\text{N}_x$) reference that exhibits only a small shoulder absorption in visible light region [16]. The x-ray photoelectron spectroscopy (XPS) spectra in Fig. S2 of PbTiO_3 powders and nanotube array for Pb 4f and Ti 2p doublets indicate the expected binding energies corresponding to PbTiO_3 . Hence, the characterization results confirm the formation of highly uniform arrays of PbTiO_3 nanotubes on FTO with Pt decorating only inside surface of the nanotubes as discussed below.

3.2. Photoelectrochemical water splitting

Photoelectrochemical measurements of particulate PTO, NT-PTO, or PNT-PTO photoanodes were carried out with a standard three-electrode configuration; a photoanode as the working electrode, Pt wire as the counter electrode, and Ag/AgCl as the reference electrode under visible light irradiation ($\lambda > 420$ nm). As shown in photocurrent density (I)–potential (V) curves Fig. 4a, the PbTiO_3 powder photoelectrode displays a meager photocurrent of $8 \mu\text{A}/\text{cm}^2$ at 1.05 V_{RHE} , which increases to $18 \mu\text{A}/\text{cm}^2$ for NT-PTO photoanode. The Pt-nanodots deposited PNT-PTO electrode shows dramatically (8 times) improved photo-activity around $64 \mu\text{A}/\text{cm}^2$ at 1.05 V_{RHE} demonstrating their pronounced promotional effect on PEC water oxidation. The photocurrents generated from PTO-PNT photoanode show a plateau between 0.85 V_{RHE} and 1.05 V_{RHE} , but a sudden increase around 1.1 V_{RHE} . This unusual when considering that the electrochemical water oxidation usually takes place above 1.6 V_{RHE} . Then, cyclic voltammetry was conducted by using a Pt wire electrode in 1 M KOH solution. In Fig. S3a, an anodic peak around 1.1 V_{RHE} is observed, which is usually attributed to Pt oxidation by adsorption of OH^- [21]. Also, the I–V curve of PNT-PTO over a wide range of potentials (0–1.8 V_{RHE}) demonstrates that the sudden increase of photocurrent around 1.1 V_{RHE} is an event taking place around the specific potential (Pt oxidation by OH^-) and has nothing to do with the oxygen evolution reaction that is observed above 1.6 V_{RHE} .

It is further noted in Fig. 4a that there are cathodic currents for potentials below ~0.7 V. This can be attributed to an efficient electron transfer from the conduction band of PbTiO_3 to chemically adsorbed oxygen molecules, the density of which is vastly increased in alkaline solutions through a charge-transfer interaction between surface anionic groups such as Ti-O^- as an electron donor and oxygen molecules as an electron acceptor. The equilibrium redox potential for the O_2 reduction in alkaline solution ($\text{O}_2 + 2\text{H}_2\text{O} + 4\text{e}^- \rightarrow 4\text{OH}^-$) is 0.26 V vs. Ag/AgCl at pH 13 [22].

Chronoamperometric characteristics of these photoelectrodes in Fig. 4b, indicates that the PNT-PTO electrode generates the highest photocurrent density of $> 60 \mu\text{A}/\text{cm}^2$ at 1.02 V_{RHE} that remains stable under chopped light irradiation. In addition, the PNT-PTO electrode shows sluggish photocurrent decay when light is turned off. The apparently longer carrier lifetime strongly implies a more efficient charge separation of the electrode. The determined IPCE in Fig. 4c shows the similar trend that is also consistent with the light absorption spectra of the three photoanodes. This indicates that the measured photocurrents originate from the photons absorbed by band-to-band electron transition. The photographs of actual electrode used for IPCE measurements are displayed in inset.

Fig. 4d shows the amounts of evolved H_2 and O_2 gases, which were measured in a closed circulation PEC system with Pt-dots@ PbTiO_3 nanotubes electrode under visible light illumination at a bias potential of 1.02 V_{RHE} . The stoichiometric amounts of both H_2 and O_2 gases are generated in the ratio close to 2 as expected from the overall water splitting reaction. The Faradic efficiency is close to unity, namely, the amounts of the gaseous products are similar to the expected amounts calculated from the generated photocurrents throughout the whole

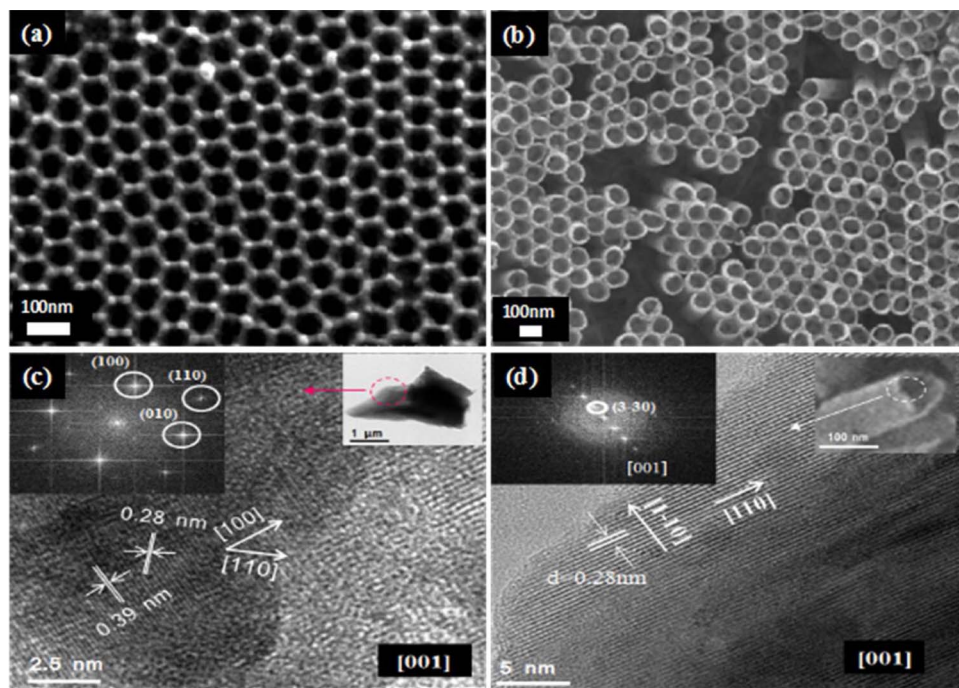


Fig. 2. FESEM images of AAO template (a) and Pt-dot deposited PbTiO₃ nanotube array (b) formed on FTO. HR-TEM images of particulate PbTiO₃ (c) and PbTiO₃ nanotube (d) along with the respective electron diffraction patterns.

measurements. Thus, most of the photo-induced charges contribute to water splitting reaction. No change in the slope of the gas evolution-time curves and the reproduction of the similar gas evolution-time curves after evacuation of accumulated gas products demonstrate that PNT-PTO photoanode is stable in the current PEC water splitting reaction [17]. Furthermore, H₂ and O₂ gas evolution rates for the various photoanodes are summarized in Table S1, indicating that 20 wt% of Pt electrode yields the highest photocurrent among PNT-PTO photoanodes of different wt% of loaded Pt. Also, the rates of H₂/O₂ evolution on the PNT-PTO electrode (20 wt% Pt) are ~7.3 times higher than those of the PbTiO₃ powder electrode and the result is in line with Fig. 4a. We also have taken TiO_{2-x}N_x as the reference material for PEC water splitting under visible light because it is also derived from TiO₂ [16], instead of other better-known metal oxide photoanode materials like BiVO₄, Fe₂O₃ and WO₃ [18]. Its absorption spectrum in Fig. 3b shows only small visible light absorption induced by N-doping into TiO₂ lattice.

4. Discussion

Band structure of cubic perovskite PbTiO₃ (*Pm3m*, *a* = 3.887 Å in the inset) calculated by density functional theory (DFT) was reported previously [19]. Yet, we also performed DFT calculation with the full potential linearized augmented plane-wave (FP-LAPW) method as implemented in the WIEN97 code in generalized gradient approximation

(GGA). The resulting density of state (DOS) functions for total crystal and contributions of individual atomic orbitals are presented in Fig. S4. The valence band is derived mainly from O 2p, but a significant contribution from Pb 6s as well. The conduction band is mainly constituted by Ti 3d. As mentioned already, the hybridization of O 2p and Pb 6s pushes up the top of the valence band and thereby forms a relatively small band gap that can absorb visible light [9,10]. At this point it may be noted that computed gap between valence and conduction band is smaller than experimental value. This is well known shortcoming of GGA formalism. Nonetheless our interest remains in understanding the role of Pb orbitals. The calculated band structure is also consistent with the schematic band structure in Fig. 5 derived from Mott-Shottky plot (conduction band position) and UV-vis absorption spectrum in Fig. 3b (a band gap of 2.78 eV). The Mott-Schottky plot of 1/C² vs. potential gives the flat band potential (V_{fb}) and the charge carrier density (N_d) of the semiconductor from x-intercept and slope, respectively, according to the equation [15,17].

$$\frac{A^2}{C_{sc}^2} = \frac{2}{e \epsilon \epsilon_0 N_d} [(V - V_{fb}) - \frac{kT}{e}]$$

where A is the electrode surface area, C_{sc} is the space charge layer capacitance, e is the electron charge, ε is the dielectric constant, ε₀ is the permittivity of vacuum, V is the potential applied to the electrode, k is the Boltzmann's constant, and T is the temperature. As shown in

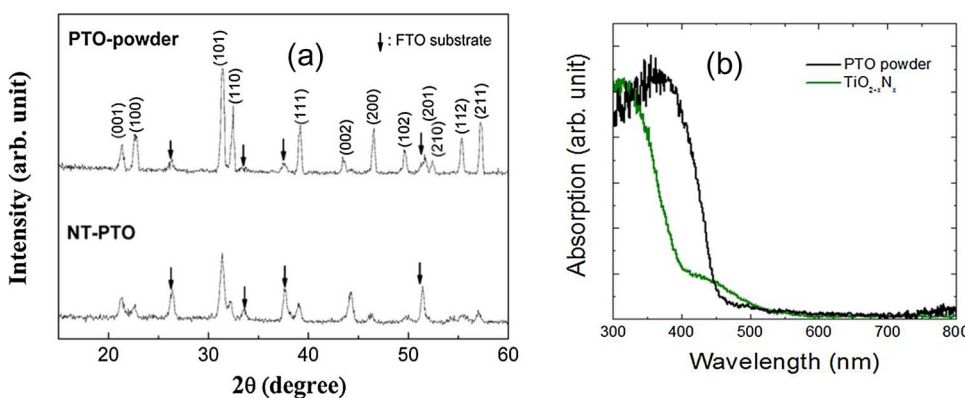


Fig. 3. (a) X-ray diffraction patterns of powder and nanotubes of PbTiO₃ (PTO). (b) UV-vis absorption spectrum of PbTiO₃ powders showing the absorption edge of 446 nm corresponding to a band gap energy of 2.78 eV. It is compared with N-doped TiO₂ (TiO_{2-x}N_x) powders.

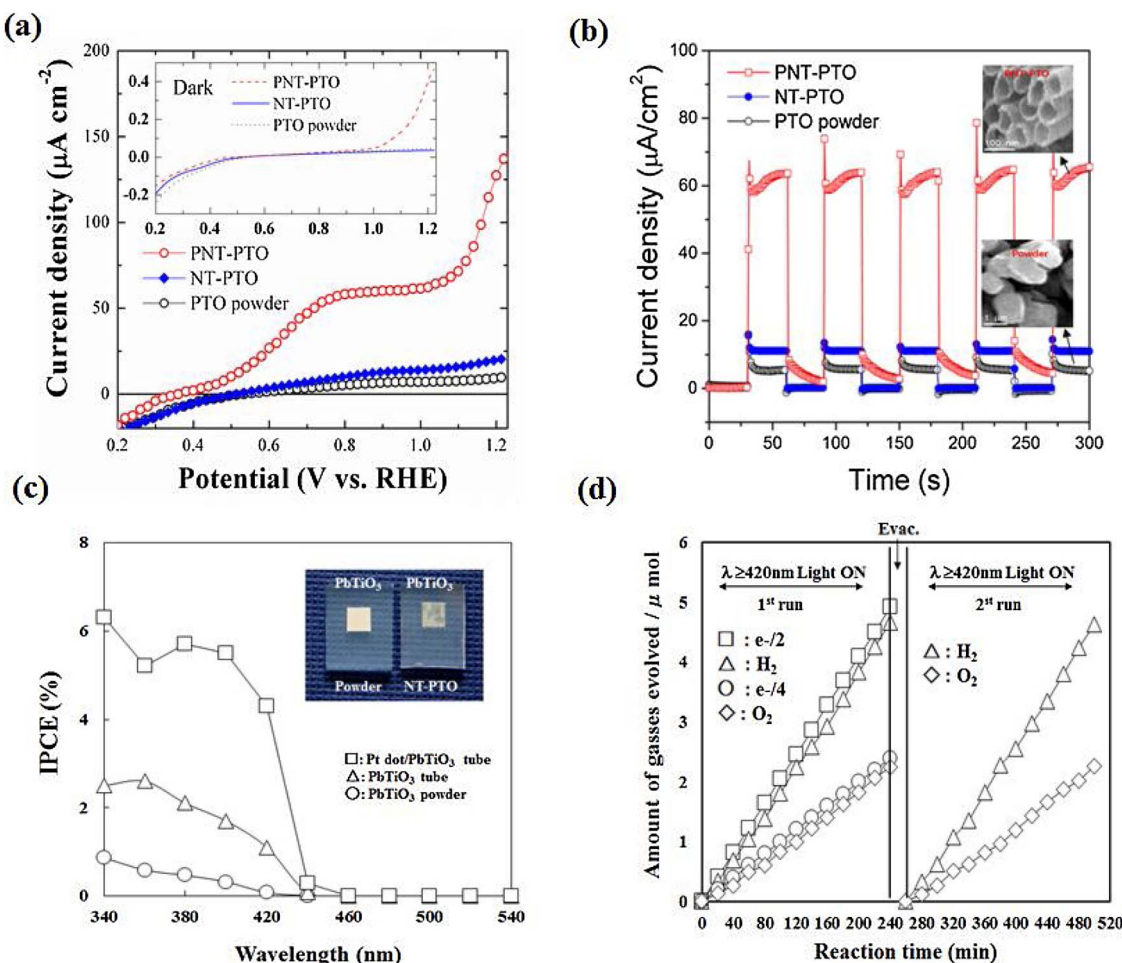


Fig. 4. (a) Photocurrent density (J)–potential (V) curves of PbTiO_3 photoelectrodes. (b) Chronoamperometric curves at applied potential of $1.02 \text{ V}_{\text{RHE}}$ under chopped irradiation. (c) IPCE curves of photoanodes and their photographs in inset. (d) Amounts of H_2/O_2 evolved. All measurements were performed under visible light ($\lambda > 420 \text{ nm}$) irradiation obtained by using an optical filter along with a 300 W Xe-lamp.

Fig. 5, the extrapolating the linear portion of the Mott-Schottky plot to x -axis yields the flat band potential of Pt-dots@ PbTiO_3 nanotube arrays electrode (0.33 V) that is very close to the conduction band edge of the n -type semiconductor. Thus obtained schematic band diagram indicates that the electrode has suitable band edges for redox reactions of water splitting.

The theoretical and experimental considerations of the band structure show the origin of the small band gap of PbTiO_3 suitable for visible light photocatalysis, which is rare among titanates. Also IPCE plot in Fig. 3c indicates that the extended light absorption into the visible light region of the PbTiO_3 photoelectrodes is converted to photocurrents at the wavelengths of absorbed photons. However, the generated

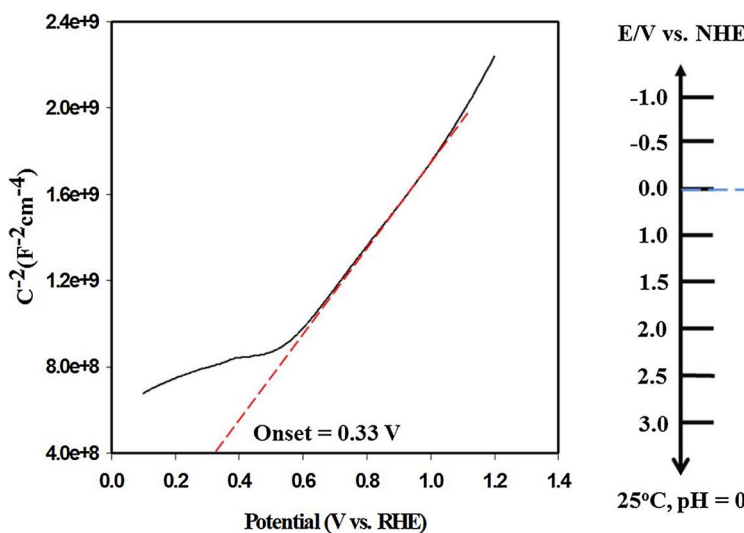
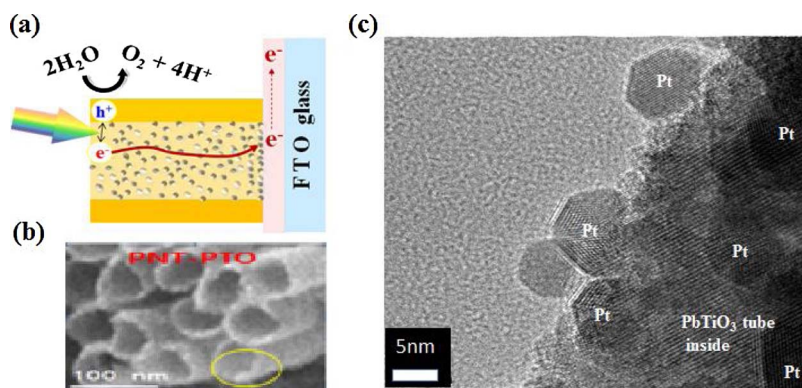


Fig. 5. Mott-Schottky plot of Pt-dots@ PbTiO_3 nanotube arrays and the band structure model based on the measured flat band potential.



photocurrents are widely different depending on the nature of PbTiO_3 photoanodes. Thus, the nanotube configuration (NT-PTO) yielded somewhat enhanced performance relative to PTO powders, but the Pt nanodots infiltration in PbTiO_3 nanotube core (PNT-PTO) dramatically improved the performance further.

The notable effect of nano-engineering could be understood based on the scheme displayed in Fig. 6a. Relative to the common particulate photoelectrode, the concept of PNT-PTO fabrication contains two unique components, i.e. 1-D nanotube array geometry and Pt nanodots infiltrated into only inside core of the tubes. In photoanodes for PEC water oxidation, oxygen evolution co-catalysts are commonly used like metal oxides or complexes to extract holes and assist the oxygen evolution reaction [20]. In our case, we employ electron-attracting Pt to extract electrons to the core of the NT-PTO. It should be noted that the outside surface of the nanotube is completely blocked by AAO template during the Pt infiltration step of the synthesis and thus Pt nanodots are confined only to the internal surface of the nanotube. This strategy isolates oxidation sites (by holes) at the external surface of the tube from electrons collected toward the internal surface of the nanotube and transferred to the FTO substrate. As a result, we can reduce the energy-wasteful electron-hole recombination, and enhance the efficiency of PEC water splitting. Fig. 6b clearly shows the formation of well-aligned nanotube array by FE-SEM image and Fig. 6c demonstrates that the Pt nanodots are present on the internal surface of the nanotube in the HRTEM image to support the scheme in Fig. 6a.

5. Conclusion

We have successfully fabricated the PbTiO_3 nanotube arrays over a thermally sensitive transparent conducting glass (FTO) substrate by an all solution-based, hard-templating procedure. A new concept of site isolation has been realized by Pt-sol infiltration in the internal core of deposited nanotube arrays and thus physically separating electron and hole reaction sites on the internal and external surfaces of the nanotubes, respectively. The effective charge separation leads to greatly enhanced photocurrent generation and H_2 evolution efficiencies relative to those of the particulate-type or nanotube-type photoanode without Pt infiltration. The physical site isolation through nano-engineering of the material fabrication demonstrated in the present work could offer a new strategy for preparation of high-efficiency PEC devices.

Fig. 6. (a) Schematic model displaying light absorption followed by an efficient electron-hole separation by tunneling electrons inside and holes outside of a nanotube in the Pt dots@ PbTiO_3 nanotubes photoanode. (b,c) FE-SEM and HR-TEM (circled area) images of the top of nanotube displaying the presence of Pt nanodots on the internal surface of the nanotube.

Acknowledgement

This work was supported by the Korea Basic Science Institute grant (T35434, T34439) and Climate Change Response project (2015M1A2A2074663, 2015M1A2A2056824), Korean Centre for Artificial Photosynthesis (NRF-2011-C1AAA0001-2011-0030278), the Basic Science Grant (NRF-2015R1A2A1A10054346) funded by MSIP, and Project No. 10050509 and KIATN0001754 funded by MOTIE of Republic of Korea.

References

- [1] B.H. Kim, M.J. Hackett, J. Park, T. Hyeon, Chem. Mater. 26 (2014) 59.
- [2] W. Lee, S.-J. Park, Chem. Rev. 114 (2014) 7487.
- [3] J.D. Holladay, J. Hu, D.L. King, Y. Wang, Catal. Today 139 (2009) 244.
- [4] A. Fujishima, K. Honda, Nature 238 (1972) 37.
- [5] I.E. Castelli, T. Olsen, S. Datta, D.D. Landis, S. Dahl, K.S. Thygesen, K.W. Jacobsen, Energy Environ. Sci. 5 (2012) 5814.
- [6] (a) S. Huang, Y. Lin, J.-H. Yang, Y. Yu, Nanotechnology for sustainable energy vol. 1140, American Chemical Society 219 (2013).
- [7] F. Fresno, Design of Advanced Photocatalytic Materials for Energy and Environmental Applications, in: M.J. Coronado, F. Fresno, D.M. Hernández-Alonso, R. Portela (Eds.), Springer London, London, 2013, p. 123.
- [8] (a) R. Ranjan, A.K. Kalyani, R. Garg, P.S.R. Krishna, Solid State Commun. 149 (2009) 2098.
- [9] H.G. Kim, O.S. Becker, J.S. Jang, S.M. Ji, P.H. Borse, J.S. Lee, J. Solid State Chem. 179 (2006) 1214.
- [10] H.G. Kim, D.W. Hwang, J.S. Lee, J. Am. Chem. Soc. 126 (2004) 8912.
- [11] K. Zhu, N.R. Neale, A. Miedaner, A.J. Frank, Nano Lett. 7 (2007) 69.
- [12] F. Yan, Y. Wang, J. Zhang, Z. Lin, J. Zheng, F. Huang, ChemSusChem 7 (2014) 101.
- [13] K.H. Reddy, K. Parida, ChemCatChem 5 (2013) 3812.
- [14] V.E. Sandana, D.J. Rogers, F. Hosseini Teherani, P. Bove, R. McClintock, M. Razeghi, Proc. SPIE 8987 (2014) 89872P, <http://dx.doi.org/10.1117/12.2057620>.
- [15] H.G. Kim, P.H. Borse, J.S. Jang, C.W. Ahn, E.D. Jeong, J.S. Lee, Adv. Mater. 23 (2011) 2088.
- [16] R. Asahi, T. Morikawa, T. Ohwaki, K. Aoki, Y. Taga, Science 293 (2001) 269–271.
- [17] (a) J.H. Kim, J.H. Kim, J.-W. Jang, J.Y. Kim, S.H. Choi, G. Magesh, J. Lee, J.S. Lee, Adv. Energy Mater. 5 (2015) 140193.
- [18] (a) P.H. Borse, H. Jun, S.H. Choi, S.J. Hong, J.S. Lee, Appl. Phys. Lett. 93 (2008) 173103.
- [19] S. Pisikunov, E. Heifets, R.I. Egilits, G. Borstel, Comp. Mater. Sci. 29 (2004) 165.
- [20] J.H. Kim, J.W. Jang, H.J. Kang, G. Magesh, J.Y. Kim, J.H. Kim, J. Lee, J.S. Lee, J. Catal. 317 (2014) 126.
- [21] M. Favaro, C. Valero-Vidal, J. Eichhorn, F.M. Toma, P.N. Ross, J. Yano, Z. Liu, E.J. Crumlin, J. Mater. Chem. A 5 (2017) 11634.
- [22] A. Tsujiko, H. Itoh, T. Kisumi, A. Shiga, K. Murakoshi, Y. Nakato, J. Phys. Chem. B 106 (2002) 5878.